**RESEARCH ARTICLE**

# Deposition of inhaled nanoparticles in the rat nasal passages: Dose to the olfactory region

Guilherme J. M. Garcia, and Julia S. Kimbell

*The Hamner Institutes for Health Sciences, Research Triangle Park, NC*

**Abstract**
In vivo experiments have shown that nanoparticles depositing in the rat olfactory region can translocate to the brain via the olfactory nerve. Quantitative predictions of the dose delivered by inhalation to the olfactory region are needed to clarify this route of exposure and to evaluate the dose-response effects of exposure to toxic nanoparticles. Previous in vivo and in vitro studies quantified the percentage of inhaled nanoparticles that deposit in the rat nasal passages, but olfactory dose was not determined. The dose to specific nasal epithelium types is expected to vary with inhalation rate and particle size. The purpose of this investigation, therefore, was to develop estimates of nanoparticle deposition in the nasal and, more specifically, olfactory regions of the rat. A three-dimensional, anatomically accurate, computational fluid dynamics (CFD) model of the rat nasal passages was employed to simulate inhaled airflow and to calculate nasal deposition efficiency. Particle sizes from 1 to 100 nm and airflow rates of 288, 432, and 576 ml/min (1, 1.5, and 2 times the estimated resting minute volume) were simulated. The simulations predicted that olfactory deposition is maximum at 6–9% of inhaled material for 3- to 4-nm particles. The spatial distribution of deposited particles was predicted to change significantly with particle size, with 3-nm particles depositing mostly in the anterior nose, while 30-nm particles were more uniformly distributed throughout the nasal passages.

**Keywords:** *CFD simulation; epithelial map; nasal filtration; nanoparticle toxicology; olfactory epithelium; particle deposition; rat nose; risk assessment*

## Introduction

The toxicity of airborne nanoparticles is under increasing scrutiny. Engineered nanoparticles (e.g., carbon nanotubes, metallic nanoparticles, quantum dots) have many potential industrial applications, but they may also represent a health hazard. Nanoparticles can remain suspended in air as primary particles (i.e., not agglomerated) at concentrations of $10^6$ particles/cm$^3$ for 30 min, which means that people may be exposed even at locations far from the generation source (Hinds, 1999). A recent laboratory study using rats showed that nanoparticles can be toxic to the central nervous system because particles depositing in the olfactory region can translocate to the brain along the olfactory nerves (Oberdorster et al., 2004). This toxicity pathway has not been shown in humans yet, but it is a plausible route of exposure for workers in some occupations. For example, welders working with manganese fume sometimes develop a Parkinson-like neurological disorder

(Antonini et al., 2006). To better understand the toxicity of inhaled nanoparticles in rats, and to extrapolate these observations from rats to humans, it is essential to characterize the fate of inhaled nanoparticles in the respiratory tract of both rats and humans. Here we use a computational model of the rat nasal passages to calculate the dose of nanoparticles deposited in the nasal and, particularly, olfactory regions of the rat as a function of particle size and breathing rate.

In vivo and in vitro experiments of particle deposition in the rat nose have been reported for particle diameters ranging from 5 nm to 10 μm (Cheng et al., 1990; Gerde et al., 1991; Kelly et al., 2001a, 2001b; Raabe et al., 1988; Schmid et al., 2008; Wolff et al., 1984; Wong et al., 2008). These experiments revealed two distinct physical regimes governing the fate of particles within the nose: Inertia governs deposition of micrometer-sized particles, while Brownian diffusion governs deposition of nanoparticles. Nasal deposition

http://www.informahealthcare.com/iht

is less than 10% for 0.5 μm particles, assuming a particle density of 1 g/cm³ and a resting minute volume of 250 ml/s (Kelly et al., 2001a, 2001b; Raabe et al., 1988). Deposition increases rapidly as particle inertia increases, reaching nearly 100% deposition for 10-μm particles. Nasal deposition of 5-nm particles is estimated to be approximately 60%, decreasing to approximately 5% for 100-nm particles due to the decreased Brownian motion of larger particles (Cheng et al., 1990; Gerde et al., 1991; Wolff et al., 1984; Wong et al., 2008). Although these studies describe how total nasal deposition varies with particle size and breathing rate, the dose to the rat olfactory region was not evaluated.

Estimating the olfactory dose of inhaled nanoparticles through in vivo or in vitro experiments is challenging due to the complex geometry of the rat nasal passages and the difficulty of performing accurate measurements for particle sizes with low nasal deposition. Fortunately, computational models of the rat nose are available, making it possible to estimate nasal deposition under various scenarios of particle size and inhalation rate. Kimbell and collaborators developed an anatomically correct, computational fluid dynamics (CFD) model of a F344 rat nose and used it to investigate airflow patterns during inspiration (Kimbell et al., 1993, 1997). Their computer simulations revealed that less than 20% of inhaled air reaches the olfactory region, while the bulk of airflow travels ventrally, going directly to the nasopharynx (Kimbell et al., 1997). These airflow patterns were compared to streamlines in water–dye experiments using nasal casts and a good agreement was found between simulations and experiments (Kimbell et al., 1993, 1997). Later this model was used to investigate nasal uptake of toxic gases, such as formaldehyde and hydrogen sulfide (Kimbell et al., 2001a, 2001b; Kimbell & Subramaniam, 2001; Schroeter et al., 2006). Such analyses are important to determine the dose-response relationship of inhaled toxic gases.

Computer models of nasal airflow in the Sprague-Dawley rat were recently reported by Minard and coworkers (Minard et al., 2006) and Yang and colleagues (Yang et al., 2007a, 2007b). The airflow patterns reported in these studies were in good agreement with those reported by Kimbell et al. for the F344 rat (Minard et al., 2006; Yang et al., 2007). Yang and colleagues (2007) also investigated the deposition of odorant molecules in the rat olfactory region. They predicted that highly water-soluble odorant molecules are absorbed mostly in the anterior nose, while odorant molecules with low water solubility have a more uniform absorption along the nasal mucosa. These authors also predicted that olfactory deposition of odorant molecules is smaller during expiration than during inspiration because airflow fraction to the olfactory region is smaller during expiration.

In this article we report estimates of nanoparticle deposition in the rat olfactory region. Nasal filtration of 1- to 100-nm particles is investigated using the CFD model of the entire F344 rat nasal passages developed by Kimbell and collaborators (Kimbell et al., 1993, 1997). Curve fittings are provided so that nasal and olfactory deposition can be estimated for particle sizes and airflow rates that were not simulated. We also describe how the locations where particles deposit depend on particle size and airflow rate. These estimates will be useful in assessing the toxicity and the dose-response relationship of inhaled nanoparticles.

## Methods

### *Description of the computational model*

The anatomical reconstruction of the rat nasal passages employed in this study was developed in earlier studies (Kimbell et al., 1993, 1997) and its development is summarized here briefly. The nasal cavity of an 18-wk-old, male F344 rat (body mass = 315 g) was fixed in formalin and embedded in a large block of acrylic resin. This block was later sectioned from the nostrils to the nasopharynx in 50-μm intervals. Photographs of these sections were taken and tracings of the airway perimeters of the right nasal passage were digitally scanned. Using in-house software, a three-dimensional computational reconstruction of the right nasal passage was obtained. This reconstruction was accomplished in two consecutive efforts: The anterior part of the nose was built first (Kimbell et al., 1993) and then the remainder of nose was added in a subsequent study (Kimbell et al., 1997). The model extends from the nostrils to the nasopharynx, including all the complex anatomy of the main nasal passages. In addition, it includes the maxillary sinus, but excludes the other paranasal sinuses (Kimbell et al., 1997).

In a previous study (Andersen et al., 1999), the four types of nasal epithelium (squamous, transitional, respiratory, and olfactory) were identified using light microscopy on histological slides prepared using hematoxylin and eosin (H&E) staining. The location of each epithelium type was mapped onto the surface of the three-dimensional (3D) computational mesh representing the rat nasal passages. The final result was a 3D, anatomically accurate reconstruction of the right nasal passage of a F344 rat with a surface map localizing the four epithelium types (see Figure 1 and Table 1). The original model was a mesh with 112,000 brick-shaped (hexahedral) elements.

For the present study, the original computational mesh of the rat nasal passages (Kimbell et al., 1997; Andersen et al., 1999) was imported into the commercial software ICEM-CFD (ANSYS, Inc., Canonsburg, PA), where the surface of the original mesh was used to produce a tetrahedral mesh with higher mesh density. The conversion from a hexahedral to a tetrahedral mesh was needed because we are progressively migrating our models from older CFD software (FIDAP) to newer platforms (Fluent). ICEM-CFD allowed for smoothing the boundaries between different epithelial types in areas where these boundaries were irregular in the original hexahedral mesh. This slight modification did not affect the three-dimensional nasal geometry, nor did it affect significantly the surface area of each epithelium type. The simulations reported here
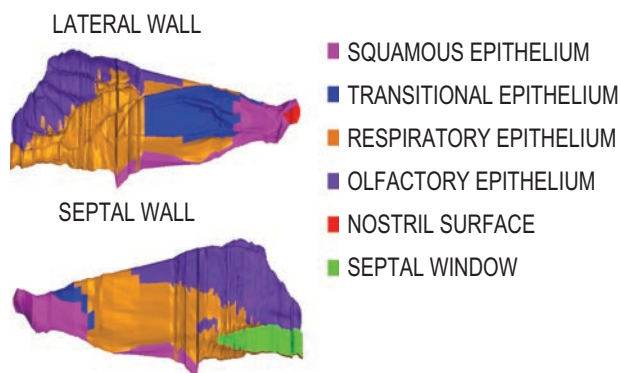
LATERAL WALL

SEPTAL WALL

- ■ SQUAMOUS EPITHELIUM
- ■ TRANSITIONAL EPITHELIUM
- ■ RESPIRATORY EPITHELIUM
- ■ OLFACTORY EPITHELIUM
- ■ NOSTRIL SURFACE
- ■ SEPTAL WINDOW

**Figure 1.** Computational geometry and epithelial map of the right nasal passage of the F344 rat. The nostril surface is displayed in red, while the septal window (symmetry plane in the nasopharynx) is displayed in green. (See colour version of this figure online at www.informahealth-care.com/iht).

**Table 1.** Surface area of the four nasal epithelium types in the F344 rat computational model (right nasal passage only).

| Epithelial type | Computational model [a] | | Experiments [b] |
| --- | --- | --- | --- |
| | Surface area | Percentage of surface area | Percentage of surface area |
| Squamous epithelium | 92.7 mm² | 10.2% | 3 ± 1% |
| Transitional epithelium | 103.6 mm² | 11.3% | — |
| Respiratory epithelium | 345.7 mm² | 37.9% | 46 ± 3% |
| Olfactory epithelium | 370.8 mm² | 40.6% | 50 ± 6% |
| TOTAL | 912.8 mm² | 100.0% | 100% |

*Note.* The distribution of epithelial types in the model is compared to experimental results reported in the literature.

[a]The distribution of epithelial types in the model was based on the histology diagrams by Mery et al. (1994).

[b]Histological measurements by Gross et al. (1982). The tip of the nose was excluded from this study, so that these numbers are expected to underpredict the percentage of surface area lined with squamous epithelium and overpredict the percentage of surface area lined with respiratory and olfactory epithelia.

were performed in a mesh with 3.2 million tetrahedral elements. A mesh density test was performed to confirm that all results were independent of mesh density. The quality of the tetrahedra was checked to ensure that all cells had an aspect ratio larger than 0.3, a value needed to avoid distorted elements and optimize the accuracy of the numerical simulations.

### Simulation methods

The dose of nanoparticles deposited in the nasal cavity and the dose deposited in the olfactory epithelium were estimated for 1- to 100-nm particles using computational fluid dynamics (CFD). CFD is an appropriate technique to quantify nanoparticle deposition in the rat olfactory region because it allows the calculation of regional doses, so that the contribution of olfactory deposition to the overall nasal deposition can be easily computed if a 3D map of the nasal epithelium types is incorporated into the model. In contrast, quantifying the olfactory dose is more challenging with in vivo and in vitro techniques due to the difficulty of distinguishing olfactory deposition from

deposition in other epithelium types, given the small size of the rat nasal passages. Another advantage of CFD modeling over in vivo and in vitro techniques is that, after the model is built, multiple particle sizes and airflow rates can be readily simulated without significant increase in labor-time and costs.

CFD simulations were conducted in Fluent (ANSYS, Inc., Lebanon, NH). Inspiratory airflow was modeled as laminar and at steady state. The assumption of laminar flow is supported by the low Reynolds number (Re) in the rat nose during resting breathing. For the airflow rates studied here, Re is in the range 121 to 242 (Kimbell et al., 1997). The assumption of laminar flow is further supported by Zhao and collaborators (2006). These authors investigated olfactory deposition of odorant particles in a human CFD model. After simulating laminar and turbulent flows, they concluded that the two models provided similar patterns of olfactory deposition for airflow rates between 300 and 1000 ml/s per nostril.

Flow field disturbances caused by the presence of nanoparticles in the flow were considered negligible. Since diffusional transport mechanisms dominate for 1- to 100-nm particles, an Eulerian approach was used for particle transport. In this approach, the trajectories of individual particles are not computed; instead, inhaled nanoparticles are modeled as a uniform mixture of particles and air, much as gas transport is modeled. Appropriate diffusion coefficients were computed from particle size (Hinds, 1999). Details of the simulation methods are described in Appendix A.

In order to assess the effects of airflow rate on deposition, simulations were performed for a series of airflow rates. The resting minute volume of the 315-g rat upon which the CFD model is based is estimated to be 288 ml/min (Kimbell et al., 2001b). Because exhalation takes half the time of a breath, average inspiratory airflow is twice the minute volume (i.e., 576 ml/min). However, only the right nasal passage is represented in our computer model, and thus the steady-state inspiratory airflow rate that corresponds to resting breathing in our model is 288 ml/min. We investigated three different inspiratory airflow rates, namely, 288 ml/min, 432 ml/min, and 576 ml/min, corresponding to 1×, 1.5×, and 2× the resting breathing rate per nostril.

### Curve fitting

Nasal deposition efficiency was plotted against particle size for each airflow rate. Curves were fitted to the data so that deposition could be estimated for other sets of parameters that were not simulated. Ingham (1991) proposed that nanoparticle deposition in the nose is a function of two non-dimensional parameters: Schmidt number, Sc, defined as $Sc = \nu/D_p$, where $\nu$ is the kinematic viscosity of air and $D_p$ is the particle diffusivity (Hinds, 1999), and $\Delta$, a diffusion parameter defined as $\Delta = D_p L/(4UR^2)$, where L is a characteristic length of the geometry, U is average inlet velocity, and R is airway radius (Zhang & Martonen, 1997). Because

RIGHTSLINK

a single nasal geometry was investigated, the parameters L and R are constant, so that nasal deposition efficiency is a function only of the particle diffusivity $D_p$ and the average velocity U. Because U is proportional to the airflow rate Q, namely, $U \sim Q/R^2$, nasal deposition in our model is a function of $D_p$ and Q alone. Total nasal deposition ($\eta$) was fitted with the equation (Cheng, 2003)

$$\eta = 1 - \exp\left[-a\frac{(D_p)^c}{Q^b}\right] \tag{1}$$

where $D_p$ is in square centimeters per second, Q is in milliliters per minute per nostril, and a, b, and c are fitted parameters. This functional form was selected because it obeys the requirement $0 \le \eta \le 1$ and provides good data fits of nasal deposition in humans (Cheng, 2003). All curve-fitting analyses were made using SigmaPlot (Systat Software, Inc., San Jose, CA).

The olfactory fraction of total nasal deposition ($F_O$) was also computed in the CFD simulations and plotted against particle size. Curves were fitted to the simulation data with the formula

$$F_O = aQ^b\exp\left[-c\frac{(D_p)^d}{Q^e}\right] \tag{2}$$

where $F_O$ is the percentage of the particles depositing in the nose that deposited in the olfactory region and a, b, c, d, and e are fitted parameters [different from those in Eq. (1)]. The term $Q^b$ was included in Eq. (2) because it provided a slightly better fit than the same functional form with b = 0.

Once the total nasal deposition efficiency ($\eta$) and the olfactory fraction ($F_O$) were calculated, olfactory deposition ($\eta_O$) was obtained by

$$\eta_O = F_O\eta \tag{3}$$

where $\eta_O$ is the fraction of inhaled nanoparticles that deposit in the olfactory region.

Hotspots of particle deposition are of particular interest in toxicology and risk assessment. To describe the spatial patterns of nanoparticle deposition, the locations of deposited particles were observed using Fluent and Fieldview (Intelligent Light, Rutherford, NJ). Different particle sizes led to different patterns of deposition within the nose. To characterize the effect of particle size on the spatial distribution of deposited particles, the wall mass flux was averaged along the perimeter of coronal cross sections and plotted as a function of the distance from the nostrils for different particle sizes.

## Results

Total nasal deposition of inhaled nanoparticles was predicted to decrease as particle size increased (Figure 2). Nasal deposition efficiency was approximately 95% for 1-nm particles, decreasing to 20% for 10-nm particles, and to 2% for 100-nm particles. Nasal deposition efficiency also varied with breathing rate. Increasing the inhalation rate reduced nasal deposition efficiency. This behavior is characteristic of diffusion-dominated particle motion, since increasing the airflow rate reduces the transit time of the particles and therefore decreases the percentage of inhaled particles that hit the wall through Brownian motion (Hinds, 1999).

Although total nasal deposition decreased for larger particle sizes (Figure 2), among the particles that deposited in the nose, the larger nanoparticles deposited at higher proportions in the olfactory region (Figure 3). Olfactory fraction of nasal deposition increased from 2% for 1-nm particles to 20% for 10-nm particles and to 35% for 100-nm particles for the resting airflow rate (288 ml/min/nostril). Increasing the airflow rate raised the olfactory fraction (Figure 3).

Olfactory deposition ($\eta_O$) was computed by multiplying total nasal deposition by the olfactory fraction of total nasal deposition (Equation (3)). Olfactory deposition was less than 10% for all particle sizes and inhalation rates (Figure 4). For
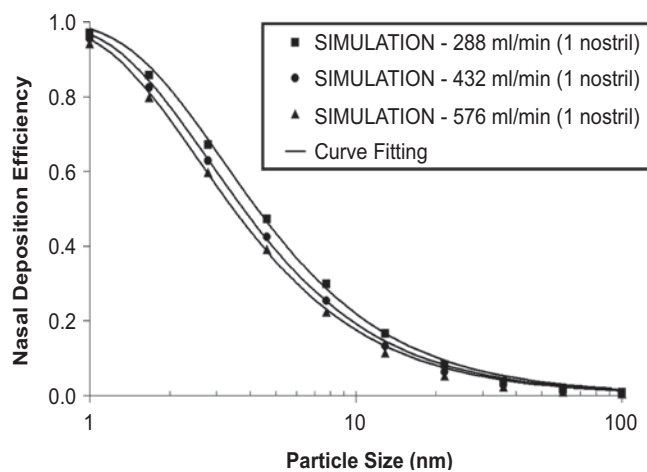
**Figure 2.** Deposition efficiency of nanoparticles in the range of 1–100 nm in the rat nasal cavity. The solid lines show the fitting obtained using Eq. (1) where a = 181 ± 49, b = 0.36 ± 0.04, and c = 0.606 ± 0.009 ($r^2$ = .9986).
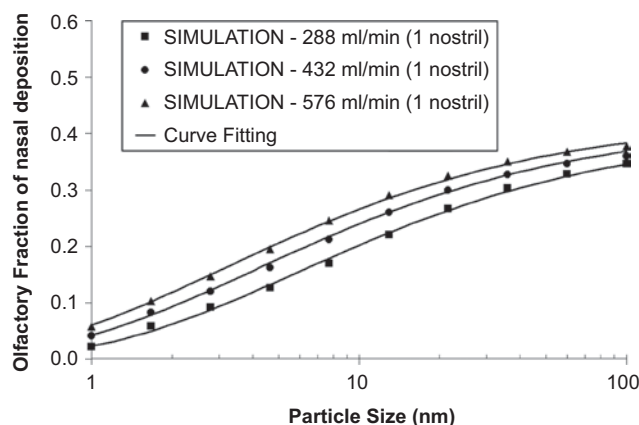
**Figure 3.** Percentage of the particles deposited in the nasal cavity that deposit in the olfactory region (Olfactory Fraction). The solid lines show the fitting obtained using Eq. (2) where a = 0.30 ± 0.04, b = 0.06 ± 0.02, c = 158 ± 46, d = 0.300 ± 0.009, and e = 0.55 ± 0.05 ($r^2$ = .9983).
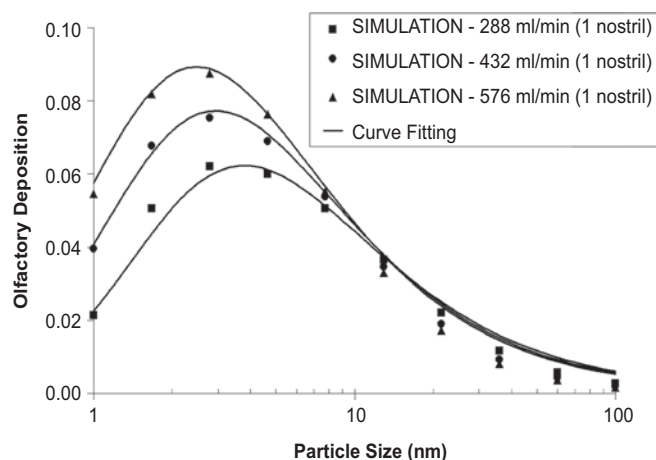
**Figure 4.** Nanoparticle deposition in the rat olfactory region as a function of particle size. The solid lines show the curves obtained using Eq. (3).

**Table 2.** Values of fitted constants and correlation coefficients ($r^2$) obtained by fitting the computational data with Eqs. (1) and (2).

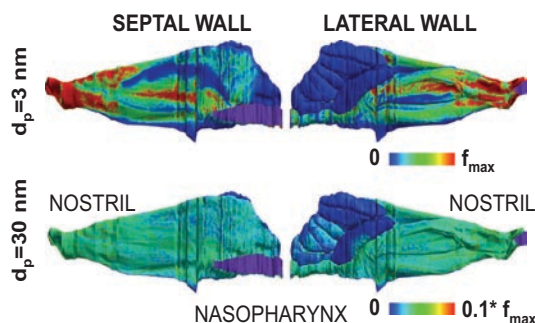|          | a         | b          | c           | d           | e        | $r^2$ |
|----------|-----------|------------|-------------|-------------|----------|-------|
| Eq. (1)  | 181 ± 49  | 0.36 ± 0.04| 0.606 ± 0.009| —          | —        | .9986 |
| Eq. (2)  | 0.30 ± 0.04| 0.06 ± 0.02| 158 ± 46   | 0.300 ± 0.009| 0.55 ± 0.05| .9983 |



**Figure 5.** Deposition patterns of 3-nm and 30-nm particles in the rat nasal cavity. While the 3-nm particles deposit preferentially in the anterior nose, 30-nm particles deposit more uniformly in the nasal passages. The scale of the color maps is specific to each particle size because there is less deposition for 30-nm particles than for 3-nm particles. The constant $f_{max}$ is not the overall maximum flux, but rather it was chosen to optimize the visualization of the deposition patterns. Values above $f_{max}$ in the 3-nm simulation and above $0.1 \times f_{max}$ in the 30-nm simulations are displayed in red. The nostril and the septal window (symmetry plane in the nasopharynx; see Figure 1) are displayed in purple. (See colour version of this figure online at www.informahealthcare.com/iht).

the resting inhalation rate, olfactory deposition increased from 2% for 1-nm particles to a maximum of 6% for 4-nm particles, decreasing to 4% for 10-nm particles, and finally decreasing to less than 1% for 100-nm particles (Figure 4). The effect of inhalation rate on olfactory deposition was non-uniform. For the smallest nanoparticles (<10 nm), olfactory deposition increased as airflow rate increased. In contrast, inhalation rate did not influence olfactory deposition of larger nanoparticles (>10 nm). The computational data was fitted to Eqs. (1) and (2), as described in the Methods section (Table 2, Figures 2–4)

It was observed that 1- to 10-nm particles deposit preferentially in the anterior nose, while 10- to 100-nm particles
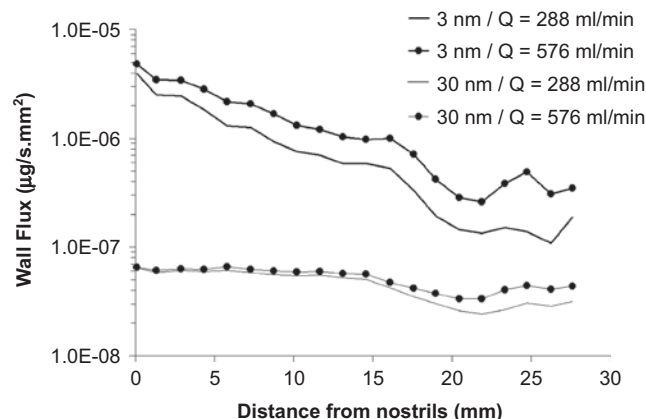


**Figure 6.** Deposition of nanoparticles in the rat nasal mucosa averaged along the perimeter of coronal cross sections and plotted as a function of the distance from the nostrils. The atmospheric nanoparticle concentration was 160 μg/m³, which is the experimental atmospheric concentration in Oberdorster et al. (2004). Curves are shown for airflow rates of 288 ml/min/nostril and 576 ml/min/nostril, corresponding to 1× and 2× the minute volume at rest, and particles sizes of 3 nm and 30 nm.

**Table 3.** Epithelial fraction of total nasal deposition and percentage of inhaled particles deposited in each epithelial type for 3-nm and 30-nm particles and airflow rates Q = 288 ml/min/nostril and Q = 576 ml/min/nostril, which correspond to 1× and 2× the airflow rate at rest.

| Epithelial fraction of total nasal deposition | | | | |
|---|---|---|---|---|
| | Q = 288 ml/min/nostril | | Q = 576 ml/min/nostril | |
| Epithelium type | 3 nm | 30 nm | 3 nm | 30 nm |
| Squamous | 37.6% | 15.8% | 30.8% | 13.9% |
| Transitional | 20.4% | 16.5% | 19.6% | 15.0% |
| Respiratory | 32.3% | 38.6% | 34.3% | 36.9% |
| Olfactory | 9.7% | 29.1% | 15.3% | 34.3% |
| Whole nose | 100% | 100% | 100% | 100% |
| Percentage of inhaled particles deposited in each epithelium type | | | | |
| | Q = 288 ml/min/nostril | | Q = 576 ml/min/nostril | |
| Epithelium type | 3 nm | 30 nm | 3 nm | 30 nm |
| Squamous | 24.2% | 0.8% | 17.4% | 0.4% |
| Transitional | 13.1% | 0.8% | 11.1% | 0.5% |
| Respiratory | 20.8% | 2.0% | 19.4% | 1.2% |
| Olfactory | 6.2% | 1.5% | 8.7% | 1.1% |
| Whole Nose | 64.3% | 5.1% | 56.6% | 3.1% |

deposit more uniformly in the nasal cavity (Figure 5). To illustrate this behavior, we considered an atmospheric nanoparticle concentration of 160 μg/m³, which is the atmospheric concentration used in the experiments of Oberdorster and colleagues (2004). The mass of nanoparticles depositing in the nasal passages was averaged along the perimeter of coronal cross sections and plotted as a function of the distance from the nostril for 3-nm and 30-nm particles (Figure 6). The 3-nm particles had a higher deposition in the anterior nose, while 30-nm particles deposited more uniformly throughout the nose (Figures 5 and 6).

This particle-size effect on the spatial distribution of deposited particles meant that the dose delivered to each epithelium type was not a constant fraction of total nasal deposition. For instance, due to its anterior location in the nose, the squamous epithelium accounted for a higher

fraction of total nasal deposition for 3-nm particles than for 30-nm particles (Table 3). As a consequence, only a small fraction of 3-nm particles reached the olfactory region, so that olfactory deposition of 3-nm particles was only 10% of total nasal deposition for Q = 288 ml/min/nostril (Table 3). In contrast, 30-nm particles had a proportionally smaller deposition in the squamous epithelium, so that olfactory deposition of 30-nm particles accounted for a larger fraction (29% for Q = 288 ml/min/nostril) of total nasal deposition.

## Discussion

The use of a three-dimensional computational model into which the olfactory region has been mapped is a cost-effective technique to quantify olfactory deposition under various scenarios of particle size and breathing rate. The computer simulations predicted the existence of a particle size, namely, 3 to 4 nm, that maximizes olfactory deposition in the rat (Figure 4). This phenomenon is a consequence of the interplay between accessibility of particles to the olfactory region and how quickly particles diffuse from the airstream to the nasal mucosa. The smallest particles (1 nm) diffuse quickly and thus are trapped mainly in the anterior portion of the nose (Figures 5 and 6). As particle size increases from 1 nm to 3 nm, filtration of particles upstream from the olfactory region decreases, and thus more particles reach the olfactory region and olfactory deposition increases (Figure 4). As particle size continues to increase beyond 3 to 4 nm, the fraction of particles reaching the olfactory region continues to rise (Figure B-2(A) in Appendix B), but olfactory deposition starts to drop because particle diffusion decreases (Figure 4).

To the best of our knowledge, this is the first study to quantify deposition of inhaled nanoparticles in the rat olfactory region. To validate our computational predictions, we compared our results to in vivo and in vitro measurements of total deposition in the nasal passages (Cheng et al., 1990; Gerde et al., 1991; Wong et al., 2008). The computational predictions are somewhat lower than the experimental measurements as shown in Figure 7 for Q = 300 ml/min/nostril (similar comparisons were obtained for other airflow rates). The diminished deposition in our study is likely due to the absence of the pharynx and larynx in the computational geometry, while the rat nasal replicas used by Cheng et al. (1990) and Wong et al. (2008) included the pharynx and larynx. Likewise, the "nasal" airway in the in vivo study by Gerde et al. (1991) included the larynx, pharynx, nasal passages, and, to some extent, the exposure mask. It is difficult to quantify precisely by how much inclusion of the pharynx and larynx in these experiments increased the deposition efficiency as compared to nasal deposition alone. In any case, the lower deposition predicted by our simulations is consistent with the geometrical differences between simulations and experiments.

Another possible explanation for the lower total nasal deposition in the simulations is that perhaps the geometry of the computational model is not as narrow as the nasal passages of live rats and replica casts used in the experiments. In order to assess this possibility, we compare in Table 4 the geometry of our model to other literature reports. The surface area of our rat CFD model (1826 mm$^2$, assuming that the left and right nasal passages are symmetrical) is somewhat larger than experimental reports (920 mm$^2$ to 1344 mm$^2$). The volume of our CFD model, 323 mm$^3$, lies between the values of 257 mm$^3$ and 400 mm$^3$ reported by
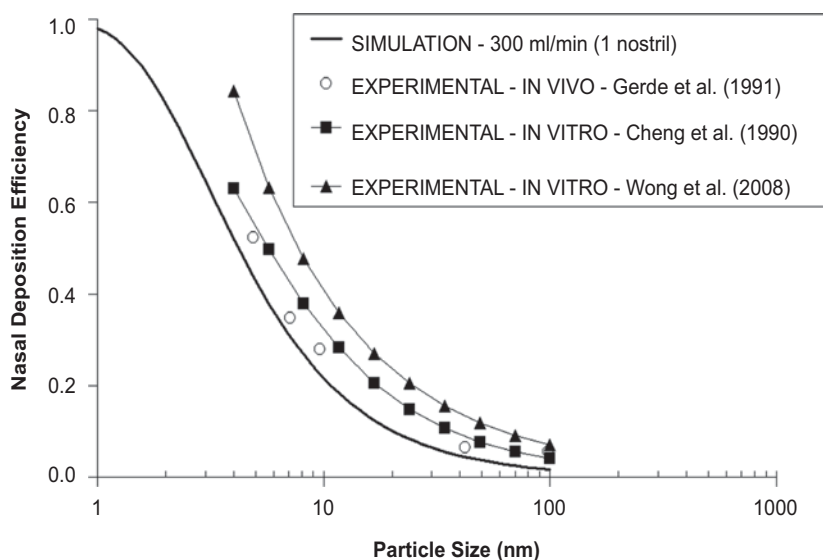


**Figure 7.** Nanoparticle deposition in the rat nasal cavity. Comparison of computational predictions and experimental results for a constant airflow rate of 300 ml/min/nostril. Deposition efficiency was estimated from fitted curves when direct measurements were not available for an airflow rate of 300 ml/min/nostril. The greater deposition efficiency in the experimental data may be due to the inclusion of the larynx and the pharynx in the nasal replicas and rats used in the experiments, while the computational domain in this study included only the nasal passages (Figure 1).

**Table 4.** Surface area and volume of the rat nose (right and left nasal cavities together) from experimental and computational investigations in the literature.

| | Surface area | Volume | Reference |
|---|---|---|---|
| **Experimental** | | | |
| F344 rat (288 g) | 1344 mm² | 257 mm³ | Gross et al. (1982) |
| F344 rat (366 g) | 920 mm² | - | Patra et al. (1987) |
| Sprague-Dawley (250 g) | 1040 mm² | 400 mm³ | Schreider (1983) |
| **Computational models** | | | |
| F344 rat (315 g) | 1826 mm² | 323 mm³ | This study[1] |
| Sprague-Dawley (500 g) | 2258 mm² | 366 mm³ | Minard et al. (2006)[2] |
| Sprague-Dawley (N/A) | 2078 mm² | 322 mm³ | Yang et al. (2007)[1,3] |

*Note.* 1, The surface area and volume of the model (right nasal passage only) were multiplied by 2, assuming that the rat nose is symmetrical. 2, Personal communication with Dr. Kevin Minard. 3, Personal communication with Dr. Kai Zhao.

Gross et al. (1982) and Schreider (1983), respectively. Both the surface area and volume of our CFD model are in good agreement with the models published by Minard et al. (2006) and Yang and collaborators (2007).

It is difficult to pinpoint a single source for the variability in surface areas and volumes reported in the literature (Table 4). The discrepancies among different studies are likely caused by multiple factors. First, the geometry of the rat nose is a function of body size and breed, which varied among the studies. Second, the extent of the nasal passages may have been defined in different ways in different studies. For instance, the tip of the nose was not included in the study by Gross et al. (1982). In addition, the boundary between the nasal passages and the nasopharynx may have been defined differently by each group of investigators. Third, each experimental report had a different anatomical resolution. Consecutive cross sections were 2 mm apart in Patra et al. (1987), 1 mm apart in Schreider (1983), and 0.5 mm apart in Gross et al. (1982). Because the surface area increased as resolution increased (Table 4), these data suggest that fine geometrical details were lost with lower anatomical resolution. The larger surface area of our model compared to the experimental reports is consistent with the higher anatomical resolution (0.05 mm apart) of the data on which the model is based. Fourth, the surface area in our model is probably somewhat inflated due to the zigzagged surface that is an artifact of the computational reconstruction (Figure 1). The same zigzagged surface also occurred in the CFD model by Yang and collaborators (2007), which explains the similarity between our values. Given all these sources of variability in the literature reports of surface area and volume, it is not possible to reach a definitive conclusion on whether the geometry of our CFD model is as narrow as the nasal passages of live rats. Nonetheless, this comparison with literature data suggests that our model is a reasonable representation of the rat nasal anatomy (Godo et al., 1994).

To further validate the computational geometry, we compared the distribution of epithelium types in the model with experimental results (Table 1). The percentage of nasal surface area lined with each epithelium type in the model, which is based on the histology diagrams of Mery and coworkers (Mery et al., 1994), is supported by the experimental observations of Gross and colleagues (1982). In particular, 41% of the surface area of the computational model is covered with olfactory epithelium, while Gross and collaborators (1982) reported that 50 ± 6% of the rat nose is lined by olfactory epithelium. The larger percentage of surface area covered with olfactory epithelium in Gross et al. (1982) may be a consequence of the exclusion of the nasal tip in their study. Inclusion of the nasal tip, which is lined with squamous epithelium, would increase the total nasal surface area and therefore decrease the percentage of area lined by olfactory epithelium.

In addition to using experimental measurements of total nasal deposition and anatomical features to validate our simulations, we can gain further insight on the spatial distribution of deposited nanoparticles from studies on olfactory uptake of odorant molecules (Yang et al., 2007). The smallest nanoparticles diffuse so rapidly that they behave essentially like a gas. The air diffusivity of 1-nm particles ($D_p = 5 \times 10^{-2}$ cm²/s; Table A-1) is similar to the air diffusivity of odorant molecules ($D_{air} \approx 6 \times 10^{-2}$ cm²/s for several odorant molecules; Yang et al., 2007). As particle size increases, particle diffusivity decreases rapidly, so that larger particles do not diffuse as rapidly as gases (Table A-1). However, besides diffusivity, the rate of absorption at the nasal wall is another parameter that plays a major role in determining the fate of inhaled material. It is generally assumed that nanoparticles are readily captured by the nasal walls upon contact. In contrast, the uptake of gases by the nasal mucosa depends on several parameters, such as gas solubility in mucus and how quickly the gas is metabolized in the nasal tissues (Taylor, 2006). Certain reactive and water-soluble gases, such as formaldehyde, are readily absorbed and metabolized by the nasal mucosa (Kimbell et al., 2001a). Other gases, such as ozone, are not metabolized as quickly, leading to a nonzero concentration in the nasal mucosa, a smaller gradient between air and tissue, and a reduced uptake rate. Gases with smaller uptake rates reach the posterior nose with higher concentrations than gases that are promptly absorbed and metabolized by the nasal mucosa. Thus, within the limits of this analogy, nanoparticles of different sizes behave somewhat like gases with different physicochemical properties (different mucus solubilities or different tissue metabolism). This analogy must be taken with caution since the mechanisms dominating the uptake of nanoparticles and gases are different: Uptake of nanoparticles is mostly governed by particle diffusivity in air (determined by particle size), while uptake of gases and odorant molecules is mostly governed by mucus solubility and tissue metabolism.

Yang and colleagues (2007) used computational models to investigate deposition of three odorant molecules

in the rat olfactory region. Carvone, an odorant with high water solubility, was strongly absorbed in the anterior nose during inspiration, while octane, an odorant with low solubility, was predicted to be more evenly absorbed throughout the nasal passages. This result is similar to our observation that 3-nm particles are mostly absorbed in the anterior nose, while 30-nm particles are more evenly absorbed throughout the nasal passages (Figures 5 and 6). Therefore, water solubility of odorants plays a role similar to particle diffusivity, so that odorants with high solubility (or nanoparticles with high diffusivity) are absorbed primarily in the anterior nose, while odorants with low solubility (or nanoparticles with low diffusivity) have a more uniform absorption throughout the nasal mucosa. The effect of airflow rate is also similar for nanoparticle deposition and odorant absorption: As airflow increases and transit time decreases, nasal deposition decreases. As discussed earlier, this analogy between nanoparticles and gases is imperfect because the mechanisms governing the uptake of nanoparticles and gases are different. Nevertheless, the comparison of our results on nanoparticle deposition with those of Yang et al. (2007) on the uptake of odorant molecules suggests that our results are qualitatively correct.

An interesting application of our olfactory deposition equations is to estimate the percentage of particles that translocate to the olfactory bulb after depositing in the olfactory region. Oberdorster and collaborators (2004) reported that 30–40 ng of particles were detected in the rat olfactory bulb within a week after a 6-h exposure to 36-nm particles at an atmospheric concentration of $160 \mu g/m^3$. By assuming that the amount of 36-nm particles depositing in the olfactory region was proportional to the airflow allocation to that region, which was estimated to be about 15% of inhaled air, Oberdorster et al. (2004) estimated that approximately 20% of the particles deposited in the olfactory region translocated to the olfactory bulb. To test the accuracy of this estimate, let us assume that the rat minute volume at rest is 214.2 ml/min to be consistent with the MPPD software used by Oberdorster et al. (2004). The mass of nanoparticles inhaled during the 6-h experiment was $(360 \, min) \times (214.2 \times 10^{-6} \, m^3/min) \times (160 \mu g/m^3) = 12.3 \mu g$. For a particle size of 36 nm and a minute volume of 214.2 ml/min ($D_p$ = particle diffusivity = $4.51 \times 10^{-5}$ cm²/s and Q = average inspiratory airflow rate = 214.2 ml/min/nostril), Eqs. (1)–(3) predict that the olfactory fraction of nasal deposition ($F_O$) is 27.5% and that the olfactory deposition ($\eta_O$) during inhalation is 1.6%. Thus, it is predicted that $0.016 \times 12.3 \mu g = 197$ ng of nanoparticles deposited in the olfactory region during the inhalation phase of the respiratory cycle. Although some olfactory deposition might also occur during expiration, the contribution of the expiratory phase is expected to be small and thus it is neglected here (see discussion below). We conclude that 15 to 20% (30–40 ng from 197 ng) of the 36-nm particles deposited in the rat olfactory region were later found in the olfactory bulb in the experiments of Oberdorster et al. (2004). It is surprising that the estimate

by Oberdorster and colleagues of 20% particle translocation from the olfactory region to the olfactory bulb is so similar to our estimate, given that they assumed $F_O = 15\%$ when in reality $F_O = 27.5\%$ for 36-nm particles. However, their underprediction of $F_O$ was compensated by the greater total nasal deposition in the earlier experimental reports in comparison to our simulation results (Figure 7). For further details on the percentage of inhaled air that flows through the olfactory region as well as further details on the filtration efficiency of the olfactory region, see Appendix B.

Finally, some limitations of this study should be noted. First, the computational results reported here were obtained for constant inspiratory airflow. Inclusion of the expiratory phase of the respiratory cycle is not expected to affect the results significantly for two reasons: (a) Any particles evading nasal filtration are likely to deposit downstream from the nose during inhalation (this is particularly true for 1- to 10-nm particles since these particles have a high diffusivity); and (b) Yang and coworkers (2007) compared the inspiratory and expiratory airflow patterns in the rat nasal passages and observed that flow through the olfactory region is lower during exhalation (for instance, for an airflow rate of 504 ml/min, expiratory flow through the olfactory region was only ~50% of the flow during inhalation). Although this reasoning suggests that olfactory dose during expiration is small, time-dependent simulations that include both the inhalation and exhalation phases of the respiratory cycle are necessary to confirm the assumption that the expiratory phase can be neglected. Second, inclusion of time-dependent changes in airflow may affect our results. In vitro and in vivo studies of micron-sized particle deposition in rats (Kelly et al., 2001a, 2001b) found somewhat greater nasal deposition for pulsating flows than for steady flows. Thus, our estimates of olfactory deposition should be used with caution when the airflow is not controlled by intubation. Future studies should compare steady versus cyclic flows to determine whether nanoparticle deposition in the rat is affected by time-dependent effects. A third limitation of this study is that our computational results are based on the nasal anatomy of a single rat. Some interindividual variability in nasal anatomy and breathing parameters is expected to occur. Nevertheless, interindividual variability should be small among inbred age-matched F344 rats. Fourth, our estimates of total nasal deposition were lower than in vivo and in vitro experimental observations (Figure 7). This underprediction of nasal deposition is consistent with the inclusion of the pharynx and larynx in the experimental models. It would be beneficial to compare computational and experimental results in models that have the same nasal geometry to verify that computational and experimental results are coincident.

## Conclusions

Quantitative estimates of nanoparticle deposition in the rat nasal passages are needed to better assess the toxicologic effects of inhaled nanomaterial. We presented CFD

RIGHTSLINK()

simulations of airflow and nanoparticle deposition in the nasal cavity of an adult F344 rat. The deposition of nanoparticles in the olfactory region was observed to vary with particle size and inhalation rate. Olfactory dose was predicted to be highest for 3- to 4-nm particles, with approximately 6 to 9% of the inhaled particles depositing in the olfactory epithelium. Curve fittings are provided so that nasal and olfactory deposition can be estimated for various particle sizes and airflow rates. These results may be useful for investigating the dose-response relationship of nanoparticle toxicity in the rat nasal cavity and, in particular, nanoparticle translocation to the brain via olfactory epithelium.

## Acknowledgements

## Note on MPPD software

The functional relationships describing how nasal and olfactory deposition vary with particle size in the rat [Eqs. (1), (2) and (3); Table 2] have been implemented in the software Multiple-Path Particle Deposition Model (MPPD). The MPPD software is copyrighted by The Hamner Institutes for Health Sciences (formerly CIIT Centers for Health Research) and RIVM (National Institute for Public Health and the Environment, the Netherlands), but it is provided free in the United States with the condition that users cite The Hamner and RIVM in any publications using dosimetry predictions obtained in MPPD. The software can be obtained by contacting Dr. Bahman Asgharian (basgharian@ara.com).

## Appendix A

Conservation of mass and momentum for laminar incompressible flow is described, respectively, by the equations

**Table A-1.** Diameter ($d_p$) and diffusivity ($D_p$) of the particles used in our simulations.

| Diameter (nm) | Diffusivity (cm²/s) |
|---|---|
| 1.00 | $5.32 \times 10^{-2}$ |
| 1.67 | $1.91 \times 10^{-2}$ |
| 2.78 | $6.91 \times 10^{-3}$ |
| 4.64 | $2.49 \times 10^{-3}$ |
| 7.74 | $9.04 \times 10^{-4}$ |
| 12.92 | $3.29 \times 10^{-4}$ |
| 21.54 | $1.21 \times 10^{-4}$ |
| 35.94 | $4.52 \times 10^{-5}$ |
| 59.95 | $1.73 \times 10^{-5}$ |
| 100.00 | $6.94 \times 10^{-6}$ |

*Note.* The 10 particle sizes were chosen so that $\log(d_p)$ is uniformly spaced along the *x* axis (see Figure 2). The particle diffusivities were calculated according to the equations in Hinds (1999).

$$\nabla \cdot \vec{u} = 0$$

$$\rho \frac{\partial \vec{u}}{\partial t} + \rho (\vec{u} \cdot \nabla) \vec{u} = -\nabla p + \mu \nabla^2 \vec{u}$$

where $\vec{u} = \vec{u}(x,y,z,t)$ is the velocity vector, $t$ is time, $\rho = 1.204\,\text{kg/m}^3$ is the air density, $p$ is pressure, and $\mu = 1.81 \times 10^{-5}$ Pa-s is the air dynamic viscosity (White, 2008). The transport of nanoparticles in air is described by the convection–diffusion equation:

$$\frac{\partial}{\partial t} C_p + (\vec{u} \cdot \nabla) C_p = D_p \nabla^2 C_p$$

where $C_p = C_p(x,y,z,t)$ is the nanoparticle concentration in air and $D_p$ is the mass diffusivity of nanoparticles in air (Hinds, 1999). The mass diffusivity $D_p$ is a function of particle size (Table A-1).

Steady-state versions of these equations were solved on a dual-processor workstation (Dell Precision, Intel Xeon 3.60 GHz, 3.93 GB of RAM) using Fluent version 6.2.16 (Fluent 6.2 User's Guide). Fluent uses the finite-volume method to solve the differential equations numerically. The segregated solver with SIMPLEC pressure–velocity coupling and second-order upwind discretization was utilized (Fluent User's Guide). Since the physical properties of the air–particle mixture were assumed constant, an uncoupled solution strategy was employed, namely, the flow field was obtained first and then the convection–diffusion equation was solved.

The boundary conditions for the fluid flow simulations were "Mass-Flow Inlet" at the nostril, "Pressure-Outlet" at the outlet ($p_{outlet} = 0$), "Wall" at the epithelial regions (squamous, transitional, respiratory, and olfactory), and "Symmetry" at the septal wall (symmetry plane in the nasopharynx; see Figure 1). For the nanoparticle deposition simulations, the concentration of nanoparticles at the nostril was set to unity ($C_p\big|_{nostril} = 1$), while the concentration was set to 0 at the walls ($C_p\big|_{wall} = 0$). The simulation results were later re-scaled to calculate wall fluxes for an inlet nanoparticle concentration of 160 µg/m³ (Figure 6).

Fluent 6.2 does not provide the option of plotting nanoparticle flux (equivalent to nanoparticle deposition; $\mathrm{Flux}_p = \left( -D_p \, \nabla C_p \right)_{\mathrm{wall}}$) at the domain walls. Therefore, a User-Defined Function (UDF) was written in Fluent to make the nanoparticle flux data available as a User-Defined Memory Variable. This UDF was used to report the fraction of nanoparticles deposited in each of the four epithelium types (squamous, transitional, respiratory, and olfactory) and to plot Figures 5 and 6. The deposition in each epithelial type obtained via the UDF was in good agreement with the fractional deposition reported by typing "report species" in Fluent's Text User Interface (TUI).

## Appendix B

For some readers it may be useful to know the concentration of nanoparticles in the air entering the olfactory region. In addition, given the swerving airways and large surface area of the rat olfactory region, it is also interesting to ask whether this region is more efficient in scrubbing nanoparticles than the nasal passages as a whole. In this appendix, we take a close look at the fate of nanoparticles carried by the olfactory stream.

The anatomy of the rat nose diverts a small percentage of inhaled air to the olfactory region, while most of the air goes directly to the nasopharynx (Figure B-1; Table B-1). In our simulations, the olfactory stream accounted for approximately 20% of inhaled air, with olfactory flow increasing slightly as the total flow increased (Table B-1). This description of the airflow distribution in the rat nose is in agreement with our previous results (Kimbell et al., 1997); the reader is referred to that earlier publication for a detailed description of the airflow patterns in the rat nasal passages.

To evaluate how effectively the olfactory region filters nanoparticles carried by the olfactory stream, we selected a cross section at the anterior end of the olfactory region
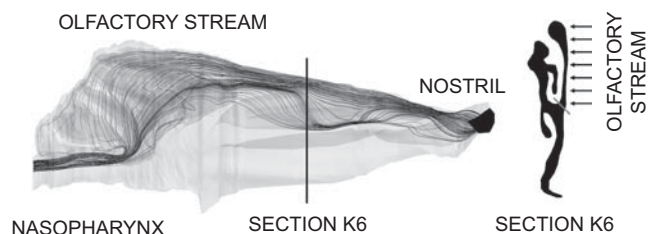


**Figure B-1.** The rat nose diverts only ~20% of inhaled air to the olfactory region, while most of the flow goes directly to the nasopharynx. Left: Lateral view of the rat nasal passages displaying olfactory streamlines for an inspiratory airflow of 288 ml/min. Right: Section K6 marks the beginning of the olfactory region (K6 corresponds to Level 6 in Kimbell et al., 1997). The olfactory stream flows through the top-right part of Section K6 as illustrated with arrows.

**Table B-1.** Airflow distribution in the rat nasal passages.

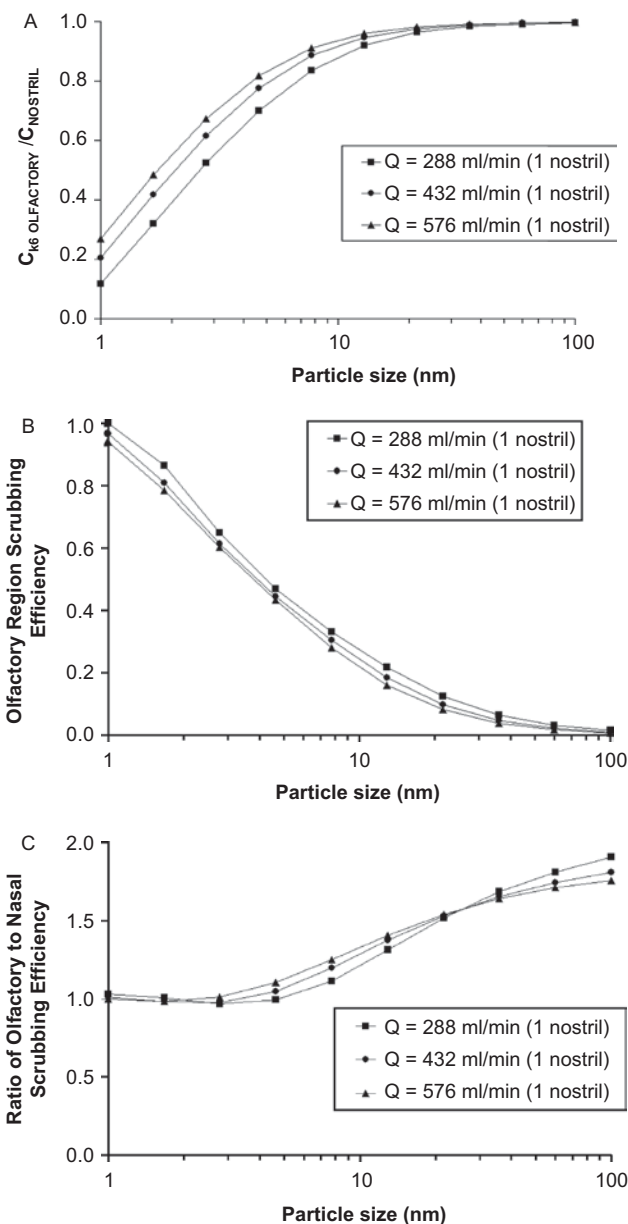| | Percentage of inhaled air | |
| --- | --- | --- |
| Airflow rate | Olfactory stream | Non-olfactory stream |
| 288 ml/min | 18.3% | 81.7% |
| 432 ml/min | 20.0% | 80.0% |
| 576 ml/min | 21.6% | 78.4% |



**FigureB-2.** Fate of nanoparticles carried by the olfactory stream. (A) Ratio of the air concentration of nanoparticles entering the olfactory region ($C_{K6\ \mathrm{OLFACTORY}}$; K6 is the cross-section defined in Figure B-1) to the concentration at the nostril ($C_{\mathrm{NOSTRIL}}$). As shown in the figure, the air concentration of nanoparticles entering the olfactory region increases with particle size. (B) Scrubbing efficiency of the olfactory region (i.e., fraction of nanoparticles entering the olfactory region that deposit in the olfactory epithelium). (C) Ratio of the scrubbing efficiency in the olfactory region to the scrubbing efficiency in the nasal passages as a whole. As shown in the figure, the olfactory region filters nanoparticles more efficiently than the rest of the nasal passages for most particle sizes.

(Section K6 in Figure B-1). The nanoparticle concentration in air was evaluated in the portion of this cross section where streamlines flow toward the olfactory region (Figure B-1, right). The simulations showed that nanoparticle concentration in air entering the olfactory region ($C_{K6\ \mathrm{OLFACTORY}}$) increased with particle size (Figure B-2(A)), which was expected due to the reduction in upstream filtration for larger particle sizes (Figure 2).

The scrubbing efficiency of the olfactory region ($\eta_{OR}$) was calculated as

$$\eta_{OR} = \frac{\text{Number of particles deposited in the olfactory region}}{\text{Number of particles entering the olfactory region}}$$

The scrubbing efficiency of the olfactory region was found to decrease with particle size (Figure B-2(B)), similarly to how total nasal deposition decreased with particle size (Figure 2). Comparing the scrubbing efficiency of the olfactory region with that of the nasal passages as a whole, we found that the olfactory region filters nanoparticles more efficiently than the nose as a whole (Figure B-2(C)). This result was expected, given the low air velocity and large surface area in the olfactory region.

# References

Andersen, M. E., Sarangapani, R., Frederick, C. B., and Kimbell, J. S. 1999. Dosimetric adjustment factors for methyl methacrylate derived from a steady-state analysis of a physiologically based clearance-extraction model. *Inhal. Toxicol.* 11:899–926.

Antonini, J. M., Santamaria, A. B., Jenkins, N. T., Albini, E., Lucchini, R. 2006. Fate of manganese associated with the inhalation of welding fumes: Potential neurological effects. Neurotoxicology 27:304–310.

Cheng, Y. S. 2003. Aerosol deposition in the extrathoracic region. *Aerosol. Sci. Technol.* 37:659–671.

Cheng, Y. S., Hansen, G. K., Su, Y. F., Yeh, H. C., and Morgan, K. T. 1990. Deposition of ultrafine aerosols in rat nasal molds. *Toxicol. Appl. Pharmacol.* 106:222–233.

*Fluent 6.2 User's Guide*. Lebanon, NH: Fluent, Inc.

Gerde, P., Cheng, Y. S., and Medinsky, M. A. 1991. In vivo deposition of ultrafine aerosols in the nasal airway of the rat. *Fundam. Appl. Toxicol.* 16:330–336.

Godo, M. N., Gross, E. A., Richardson, R. B., Joyner, D. R., Morgan, K. T., and Kimbell, J. S. 1994. Comparison of Fischer 344 rat nasal airway computational reconstruction with morphometric data. *Inhal. Toxicol.* 6(suppl.):363–366.

Gross, E. A., Swenberg, J. A., Fields, S., and Popp, J. A. 1982. Comparative morphometry of the nasal cavity in rats and mice. *J. Anat.* 135:83–88.

Hinds, W. C. 1999. *Aerosol technology: Properties, behavior, and measurement of airborne particles*. New York: Wiley-Interscience.

Ingham, D. B. 1991. Diffusion of aerosols in the entrance region of a smooth cylindrical pipe. *J. Aerosol Sci.* 22:253–257.

Kelly, J. T., Bobbitt, C. M., and Asgharian, B. 2001a. In vivo measurement of fine and coarse aerosol deposition in the nasal airways of female Long-Evans rats. *Toxicol. Sci.* 64:253–258.

Kelly, J. T., Kimbell, J. S., and Asgharian, B. 2001b. Deposition of fine and coarse aerosols in a rat nasal mold. *Inhal. Toxicol.* 13:577–588.

Kimbell, J. S., Godo, M. N., Gross, E. A., Joyner, D. R., Richardson, R. B., and Morgan, K. T. 1997. Computer simulation of inspiratory airflow in all regions of the F344 rat nasal passages. *Toxicol. Appl. Pharmacol.* 145:388–398.

Kimbell, J. S., Gross, E. A., Joyner, D. R., Godo, M. N., and Morgan, K. T. 1993. Application of computational fluid dynamics to regional dosimetry of inhaled chemicals in the upper respiratory tract of the rat. *Toxicol. Appl. Pharmacol.* 121:253–263.

Kimbell, J. S., Overton, J. H., Subramaniam, R. P., Schlosser, P. M., Morgan, K. T., Conolly, R. B., and Miller, F. J. 2001a. Dosimetry modeling of inhaled formaldehyde: Binning nasal flux predictions for quantitative risk assessment. *Toxicol. Sci.* 64:111–121.

Kimbell, J. S., Subramaniam, R. P., Gross, E. A., Schlosser, P. M., and Morgan, K. T. 2001b. Dosimetry modeling of inhaled formaldehyde: Comparisons of local flux predictions in the rat, monkey, and human nasal passages. *Toxicol. Sci.* 64:100–110.

Kimbell, J. S., and Subramaniam, R. P. 2001. Use of computational fluid dynamics models for dosimetry of inhaled gases in the nasal passages. *Inhal. Toxicol.* 13:325–334.

Mery, S., Gross, E. A., Joyner, D. R., Godo, M., and Morgan, K. T. 1994. Nasal diagrams: A tool for recording the distribution of nasal lesions in rats and mice. *Toxicol. Pathol.* 22:353–372.

Minard, K. R., Einstein, D. R., Jacob, R. E., Kabilan, S., Kuprat, A. P., Timchalk, C. A., Trease, L. L., and Corley, R. A. 2006. Application of magnetic resonance (MR) imaging for the development and validation of computational fluid dynamic (CFD) models of the rat respiratory system. *Inhal. Toxicol.* 18:787–794.

Oberdorster, G., Sharp, Z., Atudorei, V., Elder, A., Gelein, R., Kreyling, W., and Cox, C. 2004. Translocation of inhaled ultrafine particles to the brain. *Inhal. Toxicol.* 16:437–445.

Patra, A. L., Menache, M. G., Shaka, N. B., and Gooya, A. 1987. A morphometric study of nasal–pharyngeal growth for particle deposition in the rat. *Am. Ind. Hyg. Assoc. J.* 48:556–562.

Raabe, O. G., Al-Bayati, M. A., Teague, S. V., and Rasolt, A. 1988. Regional deposition of inhaled monodisperse coarse and fine aerosol particles in small laboratory animals. *Ann. Occup. Hyg.* 32:53–63.

Schmid, O., Bolle, I., Harder, V., Karg, E., Takenaka, S., Schulz, H., and Ferron, G. A. 2008. Model for the deposition of aerosol particles in the respiratory tract of the rat. I. Nonhygroscopic particle deposition. *J. Aerosol Med.* 21:291–308.

Schreider, J. P. 1983. Nasal airway anatomy and inhalation deposition in experimental animals and people. In *Nasal tumors in animals and man, Vol. III, Experimental nasal carcinogenesis*, eds. G. Reznik and S. F. Stinson, pp. 1–26. Boca Raton, FL: CRC Press.

Schroeter, J. D., Kimbell, J. S., Bonner, A. M., Roberts, K. C., Andersen, M. E., and Dorman, D. C. 2006. Incorporation of tissue reaction kinetics in a computational fluid dynamics model for nasal extraction of inhaled hydrogen sulfide in rats. *Toxicol. Sci.* 90:198–207.

Taylor, A. B. 2006. Three-dimensional computational fluid dynamics simulations of ozone uptake in the respiratory tract. PhD thesis, College of Engineering, Pennsylvania State University.

White, F. M. 2008. *Fluid mechanics*. New York: McGraw-Hill.

Wolff, R. K., Kanapilly, G. M., Gray, R. H., and McClellan, R. O. 1984. Deposition and retention of inhaled aggregate 67Ga2O3 particles in beagle dogs, Fischer-344 rats, and CD-1 mice. *Am. Ind. Hyg. Assoc. J.* 45:377–381.

Wong, B. A., Tewksbury, E. W., and Asgharian, B. 2008. Nanoparticle deposition efficiency in rat and human nasal replicas. Society of Toxicology 47th Annual Meeting. Seattle, WA.

Yang, G. C., Scherer, P. W., and Mozell, M. M. 2007a. Modeling inspiratory and expiratory steady-state velocity fields in the Sprague-Dawley rat nasal cavity. *Chem. Senses* 32:215–223.

Yang, G. C., Scherer, P. W., Zhao, K., and Mozell, M. M. 2007b. Numerical modeling of odorant uptake in the rat nasal cavity. *Chem. Senses* 32:273–284.

Zhang, Z., and Martonen, T. 1997. Deposition of ultrafine aerosols in human tracheobronquial airways. *Inhal. Toxicol.* 9:99–110.

Zhao, K., Dalton, P., Yang, G. C., and Scherer, P. W. 2006. Numerical modeling of turbulent and laminar airflow and odorant transport during sniffing in the human and rat nose. *Chem. Senses* 31:107–118.